

Ferroelectric ZrO_2 monolayers as buffer layers between SrTiO_3 and Si

Mehmet Dogan^{*1,2,3,4} and Sohrab Ismail-Beigi^{1,2,5,6}

¹*Center for Research on Interface Structures and Phenomena,
Yale University, New Haven, Connecticut 06520, USA*

²*Department of Physics, Yale University,
New Haven, Connecticut 06520, USA*

³*Department of Physics, University of California,
Berkeley, California 94720, USA*

⁴*Materials Science Division,
Lawrence Berkeley National Laboratory,
Berkeley, California 94720, USA*

⁵*Department of Applied Physics, Yale University,
New Haven, Connecticut 06520, USA*

⁶*Department of Mechanical Engineering and Materials Science,
Yale University, New Haven, Connecticut 06520, USA*

^{*}*Corresponding author: mhmtdogan@gmail.com*

(Dated: March 27, 2019)

A monolayer of ZrO_2 has recently been grown on the Si(001) surface and shown to have ferroelectric properties, which signifies the realization of the lowest possible thickness in ferroelectric oxides (M. Dogan et al., *Nano Lett.*, **18** (1) (2018) [1]). In our previous computational study, we reported on the multiple (meta)stable configurations of ZrO_2 monolayers on Si, and how switching between a pair of differently polarized configurations may explain the observed ferroelectric behavior of these films (M. Dogan and S. Ismail-Beigi, *arXiv:1902.01022* (2019) [2]). In the current study, we conduct a DFT-based investigation of (i) the effect of oxygen content on the ionic polarization of the oxide, and (ii) the role of zirconia monolayers as buffer layers between silicon and a thicker oxide film that is normally paraelectric on silicon, e.g. SrTiO_3 . We find that (i) total energy-vs-polarization behavior of the monolayers, as well as interface chemistry, is highly dependent on the oxygen content; and (ii) $\text{SrTiO}_3/\text{ZrO}_2/\text{Si}$ stacks exhibit multiple (meta)stable configurations and polarization profiles, i.e. zirconia monolayers can induce ferroelectricity in oxides such as SrTiO_3 when used as a buffer layer. This may enable a robust non-volatile device architecture where the thickness of the gate oxide (here strontium titanate) can be chosen according to the desired properties.

I. INTRODUCTION

Metal oxide thin films exhibit a diverse set of physical phenomena with technological applications, such as ferroelectricity, ferromagnetism and superconductivity, and thus have motivated intense scientific research for decades [3, 4]. One of these phenomena, thin film ferroelectricity, potentially enables non-volatile devices such as ferroelectric field-effect transistors (FEFET). In traditional field-effect transistors, the state of the device is determined by the applied gate voltage, meaning when the gate voltage is turned off, the state is also switched to “off” (hence it is volatile). In contrast, in a FEFET, the polarization of the thin film oxide can be retained, and keeps the state “on” after the gate voltage is turned off (hence it is non-volatile). Encoding the state in the oxide rather than the applied gate voltage greatly decreases the energy requirement and increases the speed of these transistors [5, 6]. Achieving this requires a metal oxide which remains (or becomes) ferroelectric as a thin film on a semiconductor, and an interface between the two materials that is atomically abrupt, causing the electronic states between them to be coupled [7–9]. The first of these prerequisites has been a primary challenge due to the fact that bulk ferroelectrics do not retain their macroscopic

polarization under a critical thickness because of the depolarizing field caused by surface bound charges [10, 11]. However, instead of focusing on bulk ferroelectrics, it is possible to engineer atomically abrupt interfaces between semiconductors and oxides such that the oxide is stable in multiple polarization states in the thin film form [9]. This approach utilizes strong interface effects to offset the depolarizing effects of the thin film’s surface. Therefore, achieving an abrupt interface between the oxide and the semiconductor is critical for both (i) coupling their electronic states, and (ii) inducing multiple polarizations in the oxide. This is challenging because of the amorphous oxide layers (such as SiO_2) that usually form at the interfacial region [6, 12, 13]. However, recent developments in the growth methods such as molecular beam epitaxy (MBE) allows us to overcome this difficulty in many materials systems [5, 14, 15].

In a recent letter, we reported on the ferroelectric behavior of atomically thin ZrO_2 grown on Si(001) [1]. This was achieved by atomic layer deposition (ALD) which produced an atomically abrupt interface and a mostly amorphous oxide. Using amorphous Al_2O_3 as a top electrode, a gate stack was created, and ferroelectric behavior was observed via $C - V$ measurements. In our following computational work, we presented an in-depth

analysis of the monocrystalline $\text{ZrO}_2/\text{Si}(001)$ interface [2]. Using Monte Carlo simulations on a discrete lattice model whose parameters are extracted from DFT results, we conducted an investigation of the multi-domain film, which approximates the experimental amorphous film. Our results suggested that two low-energy configurations of opposite polarization may be dominant in the experimental film. Thus the observed ferroelectric behavior can be understood as locally switching between these configurations.

In this work, we present a complementary computational study of the effect of oxygen content on the interface chemistry and the polarization of these monolayers, and find that oxygen content can be used to adjust the energy-vs-polarization behavior of these monolayers (section III A). In addition, we investigate epitaxial $\text{SrTiO}_3/\text{ZrO}_2/\text{Si}$ heterostructures in order to test the idea that an ultrathin binary oxide such as ZrO_2 can induce ferroelectricity in a thicker perovskite oxide, such as SrTiO_3 , when used as a buffer layer (section III B). We show that the SrTiO_3 thin films, paraelectric when grown directly on $\text{Si}(001)$ [16], possess multiple (meta)stable configurations with varying ionic polarization, in the $\text{SrTiO}_3/\text{ZrO}_2/\text{Si}$ stacks. These configurations are (meta)stable for 1.5-3.5 u.c. of SrTiO_3 . Therefore, it may be possible to utilize these stacks in a non-volatile device such as a FEFET where the thickness of the gate oxide can be changed as desired without compromising ferroelectric properties. A recent report tested a related idea, i.e. a thin layer of ZrO_2 as a buffer between $\text{Hf}_{0.5}\text{Zr}_{0.5}\text{O}_2$ and SiO_2/Si , and found that ferroelectricity in $\text{Hf}_{0.5}\text{Zr}_{0.5}\text{O}_2$ is significantly enhanced [17]. This experimental report, along with our theoretical predictions, should encourage experimental researchers to pursue this idea in a variety of materials systems.

II. COMPUTATIONAL METHODS

In order to find low-energy configurations of the systems of interest, we use density functional theory (DFT) with the Perdew–Burke–Ernzerhof generalized gradient approximation (PBE GGA) [18] and ultrasoft pseudopotentials [19]. We employ the QUANTUM ESPRESSO software package [20]. We use a 35 Ry cutoff for the energy of the plane waves used to describe the pseudo Kohn–Sham wavefunctions. The Brillouin zone is sampled with an $8 \times 8 \times 1$ Monkhorst–Pack k -point mesh (per 1×1 in-plane primitive cell) and a 0.02 Ry Marzari–Vanderbilt smearing [21]. A typical simulation cell consists of 8 atomic layers of Si whose bottom layer is passivated with H, a monolayer of ZrO_2 , 1.5-3.5 unit cells of SrTiO_3 , and in some cases, 2 atomic layers of Au (see Figure 1). The in-plane lattice constant is fixed to 3.87 Å, based on the computed lattice constant of bulk silicon. ~ 12 Å of vacuum is placed between periodic copies of the slab in

the z -direction. However, the slab may have an overall dipole moment that might interact with its periodic copies due to the long-range nature of the Coulomb law. In order to eliminate this unphysical effect, a fictitious dipole in the vacuum region of the cell is introduced so that it creates an equal and opposite electric field in vacuum [22]. All atomic coordinates are relaxed until the forces on all the atoms are less than 10^{-3} Ry/ a_0 in all axial directions, where a_0 is the Bohr radius (the exception being the bottom 4 layers of Si which are fixed to their bulk positions in order to simulate a thick Si substrate).

III. RESULTS

A. ZrO_x monolayers on $\text{Si}(001)$

The X-ray photoelectron spectroscopy (XPS) analysis presented in Ref. [1] showed that in the ZrO_x/Si interface, most of the interfacial Si atoms are in the Si^0 state, with a small portion (< 0.2 monolayer) in the Si^{1+} state. This established that the growth procedure described in Ref. [1] results in an interface without a large number of oxygen-coordinated silicon atoms. Further XPS analysis indicates that most Zr atoms are in their Zr^{4+} state with some in other oxidized states. Therefore, the experimental ZrO_x/Si interface has $x \lesssim 2$, and our previous theoretical work examined the ZrO_2 stoichiometry [2]. However, we know that the oxygen content of oxide thin films can be highly dependent on the growth conditions. In order to provide a comprehensive survey of these monolayers that may be experimentally realized through different growth methods, we have investigated ZrO_2 monolayers with varying amounts of oxygen. To this end, we have simulated interfaces with O:Zr ratios of 1.0, 1.5, 2.0, 2.5 and 3.0.

1. Low-energy structures of ZrO_x films

In Ref. [2], we presented the low-energy structures of ZrO_2 monolayers on the $\text{Si}(001)$ surface. Among the several metastable 2×1 configurations we discovered, five of them are within 1 eV (per 2×1 cell) of the lowest-energy configuration. We reported on the ionic polarizations, transition barriers and domain energetics of these configurations in Ref. [2]. To generate the initial configurations of the under- and over-oxygenated films, we take all the metastable configurations of the ZrO_2 monolayers, and either remove or add oxygens appropriately. For ZrO_x where $x = 1.0$ (1.5), we remove 2 (1) O per cell, which yields 6 (4) initial configurations for each metastable configuration of ZrO_2 . For ZrO_x where $x = 2.5$ or 3.0, we add oxygen atoms to one or two of the following four positions: between surface Si atoms along the x -direction

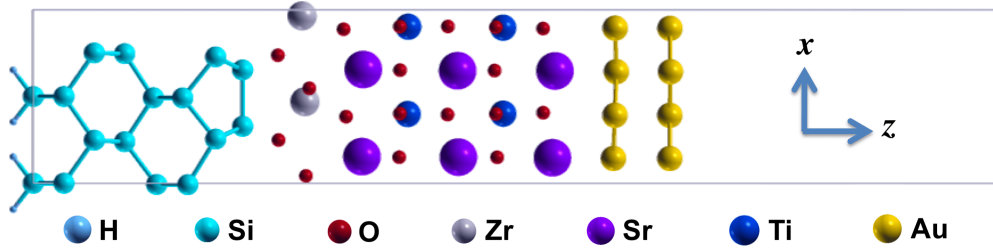


Figure 1. A typical simulation supercell of the $\text{SrTiO}_3/\text{ZrO}_2/\text{Si}$ stack with 2×1 in-plane periodicity. A two-layer Au top electrode is also included in some simulations, and is shown. The bottom 4 layers of Si are passivated by H and fixed to bulk coordinates. There is $\sim 12\text{\AA}$ of vacuum along the z -direction to separate periodic copies.

(the midpoint of a dimer and halfway between successive dimers for non- 1×1 systems), and between a surface Si atom and its neighbor in the subsurface layer (two inequivalent positions for non- 1×1 systems). These choices are suggested by previous studies of O adsorption to the bare Si(001) surface [23, 24]. We find that the most favorable position for an O atom on the Si(001) surface is the midpoint of a dimer, and the next most favorable position (higher in energy by 0.23 eV per O) is between a surface atom and its subsurface neighbor (a “back bond”). Therefore, we have four positions to add an oxygen to a 2×1 ZrO_2/Si interface, and hence 4 (6) initial configurations of $\text{ZrO}_{2.5(3.0)}$ for each metastable configuration of ZrO_2 .

After relaxing all of the configurations we have generated according to the above procedure, we have obtained a large number of metastable configurations for ZrO_x for $x = 1.0, 1.5, 2.5$ and 3.0 . In Table I we list the energies of these configurations (as well as ZrO_2), for structures that are 1 eV or less (per 2×1 cell) higher than the ground state for all x . We follow the naming convention in Ref. [2]: for a given stoichiometry, $S1$ corresponds to the ground state, $S2$ the second lowest-energy state and so on. (Thus, two $S1$ structures for two different stoichiometries are not structurally related.) We notice that the multiplicity of structures at low energies is a feature of this system independent of the oxygen content. For $x = 1.0, 2.5$ and 3.0 , the second lowest energy structure is within 0.02 eV of the ground state. See Figure 2 for the illustrations of the listed structures for $x = 2.0$, and the Supplementary Material for the other values of x .

2. Polarization and Zr-O coordination

Given the large number of structures, we are only able to describe overall statistical trends for this dataset. Our main observations are the following. (i) For the under-oxygenated cases ($x = 1.0, 1.5$), we find that structures with lower energy have fewer Si-O bonds, and on aver-

E (eV)	$S1$	$S2$	$S3$	$S4$	$S5$	$S6$
$\text{ZrO}_{1.0}$	$\equiv 0.00$	0.06	0.18	0.19	0.49	0.83
$\text{ZrO}_{1.5}$	$\equiv 0.00$	0.12	0.45	0.63	0.88	
$\text{ZrO}_{2.0}$	$\equiv 0.00$	0.07	0.14	0.50	0.69	
$\text{ZrO}_{2.5}$	$\equiv 0.00$	0.02	0.32	0.33	0.50	0.90
$\text{ZrO}_{3.0}$	$\equiv 0.00$	0.00	0.29			

Table I. Total energies of ZrO_x monolayers on Si(001), where $x = 1.0, 1.5, 2.0, 2.5, 3.0$ (reported in eV per 2×1 cell).

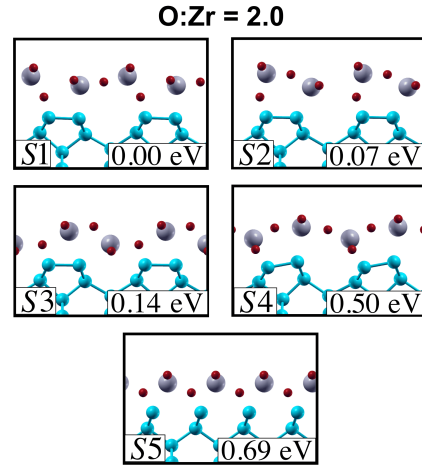


Figure 2. Low energy relaxed configurations of monolayers with $\text{O:Zr} = 2.0$. Energies are reported per 2×1 in-plane cell.

age the oxygens are farther from the Si surface than the Zr: this represents the fact that O prefers to bond to Zr over Si. (ii) For low oxygen content, we find more Si-Zr bonds forming: this happens because the Zr are not fully oxidized and prefer to donate electrons to the more electronegative Si. (iii) In the over-oxygenated cases ($x = 2.5, 3.0$), we find that the extra oxygens bond to the available sites on the Si surface and the remaining oxygens distribute themselves among the Zr atoms such that the coordination of the Zr by O is maximized.

The above observations follow from the data shown in Figure 3. On the left hand side, we plot total energy vs δz for all of the structures in our library. The quantity δz describes the ionic polarization of the ZrO_x monolayer and is defined as the mean vertical Zr-O separation: $\delta z \equiv \bar{z}(\text{Zr}) - \bar{z}(\text{O})$. A crude interpretation of this quantity suggests that the film is positively polarized when $\delta z > 0$ and vice versa. We find that negative ionic polarization is preferred for $x = 1.0, 1.5$, and that the energy increases as the polarization increases. Hence, the O anions prefer to be farther from the Si surface, and the Zr cations prefer to be closer. We find the opposite for $x = 2.0, 2.5, 3.0$, where positive polarization is preferred, and the lowest energy structures have the highest Zr-O out-of-plane separation. On the right hand side, we plot total energy vs the coordination number of Zr by O. We calculate the coordination number for a Zr atom by counting the number of O atoms within ~ 2.5 Å, which is approximately the sum of the Zr and O atomic radii. Instead of a sharp cutoff at 2.5 Å, for each Zr-O bond, we use a Fermi-Dirac function centered at 2.7 Å (“chemical potential”) and with width 0.4 Å (“temperature”) to compute coordination numbers. We then average the coordination numbers of the two inequivalent Zr atoms and report it in the figure. We find that for all O:Zr ratios, higher C.N. correlates with lower energy.

The above analysis of the ZrO_x films on Si with varying O:Zr ratios suggests that the oxygen content can be used to change the ferroelectric switching behavior of the films. Indeed, in the case of $\text{ZrO}_{2.0}$, our in-depth investigation of domain energetics indicated that the polarization switching likely occurs between $S2$ and $S3$ (see Table I [2]), which results in an energy difference of 0.07 eV and a polarization difference (change in δz) of 0.42 Å. We list the analogous values for all low-energy transitions in Table II. For example, for $\text{ZrO}_{1.5}$ ($\text{ZrO}_{2.5}$), if the switching occurred between $S1$ and $S2$, the energy difference would be 0.12 eV (0.02 eV) and the polarization difference would be 0.71 Å (0.51 Å). In the table, we only include transitions between low-energy configurations ($E_{\text{initial}}, E_{\text{final}} \leq 0.20$ eV with respect to $S1$) with a low energy difference ($|E_{\text{final}} - E_{\text{initial}}| \leq 0.15$). We observe that for $x = 1.5, 2.0$ and 2.5, there are low-energy transitions with large changes in the ionic polarization, and thus, they may be the best compositions for ferroelectric applications. It may be worth testing experimentally whether

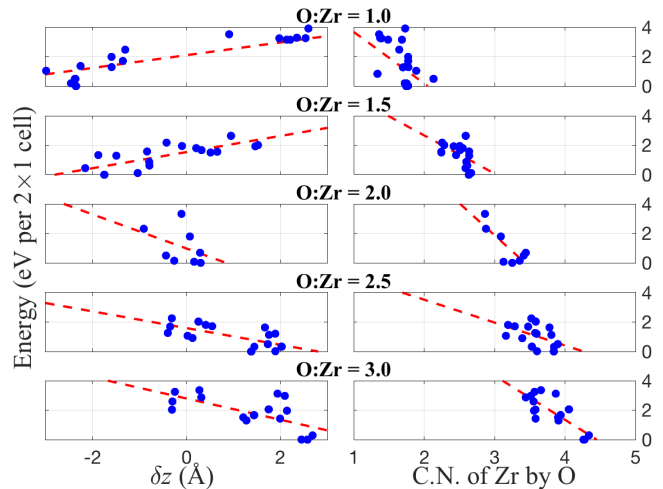


Figure 3. Scatter plots of energy E versus δz and the coordination number (C.N.) of Zr by O for the relaxed structures of the ZrO_x monolayers on Si(001), where $x = 1.0, 1.5, 2.0, 2.5, 3.0$. Linear least-squares fits are displayed as red dashed lines. The quantity $\delta z \equiv \bar{z}(\text{Zr}) - \bar{z}(\text{O})$ measures the mean ionic out-of-plane polarization. C. N. of Zr by O is defined as the number of oxygen atoms that are within ~ 2.5 Å of a zirconium atom (see text for details). For each structure, the C.N. is calculated separately for the two inequivalent Zr atoms and then is averaged over the Zr. Energies are in eV per 2×1 in-plane cell measured with respect to the lowest energy structure for each O:Zr ratio.

there is a larger ferroelectric switching in the case of $x = 1.5$ and 2.5 compared to $x = 2.0$, as suggested by our results.

3. Electronic structure of ZrO_x films

In many potential applications of the ZrO_x/Si interface such as the FEFET, an insulating interface is desired. In Table III, we list the computed band gaps of the low energy configurations of the ZrO_x/Si stacks. The maximal value of 1.0 eV is equal to the band gap of Si in the interior of the substrate, as determined by an analysis of layer-by-layer projected densities of states. We compute the band gap of bulk silicon as 0.7 eV, which is smaller than the experimental gap of 1.2 eV [25], but in agreement with other computational studies employing GGA [26]. This underestimation of the gap is expected in DFT. However, in the 8-layer thick Si slab we have used, the gap increases to 1.0 eV due to quantum confinement. We have tested this effect by varying the slab thickness in Si thin films: for 8, 12, 16 and 20 layers, we have found a band gap of 1.02, 0.94, 0.85 and 0.78 eV, respectively.

According to Table III, for $x = 1.5, 2.0$ and 2.5, the low-energy configurations are insulating with the maximal (or close to the maximal) band gap. This reinforces

	Transition	Change in E (eV)	Change in δz (Å)
ZrO _{1.0}	$S1 \rightarrow S2$	0.06	-0.08
	$S2 \rightarrow S3$	0.12	0.02
	$S3 \rightarrow S4$	0.01	0.03
	$S2 \rightarrow S4$	0.13	0.05
ZrO _{1.5}	$S1 \rightarrow S2$	0.12	0.71
ZrO _{2.0}	$S1 \rightarrow S2$	0.07	-0.15
	$S2 \rightarrow S3$	0.07	-0.42
	$S1 \rightarrow S3$	0.14	-0.57
ZrO _{2.5}	$S1 \rightarrow S2$	0.02	-0.51
ZrO _{3.0}	$S1 \rightarrow S2$	0.00	0.13

Table II. List of low-energy transitions for ZrO_x monolayers on Si(001), where $x = 1.0, 1.5, 2.0, 2.5, 3.0$, the change in energy (eV per 2×1 cell), and the change in the average cation-anion vertical displacement (Å) as a result of the transition.

the usefulness of these compositions in FEFET-related applications. We observe that for ZrO_{1.0}, the two lowest-energy configurations have a small gap and the higher-energy configurations are metallic. This is due to the under-coordination of zirconiums by oxygens and/or silicon dangling bonds. This is also the case for $S5$ of ZrO_{1.5}. Therefore a lower O:Zr ratio should be aimed for other applications in which a metallic interface is desired.

B. ZrO₂ as a buffer between SrTiO₃ and Si

The observation of ferroelectricity in the monolayer ZrO₂ on silicon marks the experimental attainment of the thinnest possible oxide ferroelectric [1, 2]. In the previous section, we have shown that under- and over-oxygenated ZrO₂ may also exhibit switchable polarization. A related goal in the field of thin film oxide/semiconductor

E_{gap} (eV)	$S1$	$S2$	$S3$	$S4$	$S5$	$S6$
ZrO _{1.0}	0.3	0.2	metal	metal	metal	metal
ZrO _{1.5}	1.0	1.0	0.7	0.7	metal	
ZrO _{2.0}	1.0	1.0	1.0	0.6	1.0	
ZrO _{2.5}	0.8	0.9	0.9	0.8	0.9	1.0
ZrO _{3.0}	0.7	0.7	0.7			

Table III. DFT band gaps of ZrO_x monolayers on Si(001), where $x = 1.0, 1.5, 2.0, 2.5, 3.0$ (reported in eV).

physics is to achieve ferroelectricity in thin perovskite films [9]. To this end, we have conducted a study of SrTiO₃/ZrO₂/Si heterostructures. Using MBE, SrTiO₃ can be grown epitaxially on Si with a small compressive strain [14, 27]. It has also been found that although SrTiO₃ is not a ferroelectric material in the bulk down to very low temperatures, a small compressive strain, attainable by epitaxy to the Si(001) surface, makes it a room-temperature ferroelectric [28]. However, the SrTiO₃/Si heterostructures grown to date have been paraelectric due to the pinning of the polarization by the interface chemistry [27, 29]. We will show below that it is possible to overcome this pinning with a buffer layer that has a richer landscape of interface chemistry, i.e. ZrO₂, and that STO/ZrO₂/Si heterostructures indeed possess multiple (meta)stable configurations with varying polarization profiles. This may enable researchers to grow oxide/semiconductor heterostructures of varying thicknesses with switchable polarization.

1. Low-energy configurations of SrTiO₃/ZrO₂/Si stacks

We find that bulk SrTiO₃ has a lattice constant of 3.93 Å, which puts it at a 1.5% compressive strain on Si(001), in agreement with previous studies [27, 29]. In order to generate initial configurations for STO/ZrO₂/Si stacks, we have begun with the relaxed coordinates of the five low-energy ZrO₂/Si interfaces, and placed a 1.5 u.c.-thick STO slab on top, laterally shifted by the vector $(\frac{n_1}{3}a, \frac{n_2}{3}a, 0)$, where $n_1, n_2 = 0, 1, 2$, and a is the lattice constant, which yields 45 initial configurations. Relaxing these 45 configurations have resulted in 6 configurations which are all local minima in the energy landscape. We

have then added more STO layers to generate 2, 2.5, 3 and 3.5 u.c.-thick slabs. Finally, to create a gate stack and to examine the effects of boundary conditions, we have added a two-layer thick gold top electrode to all of these relaxed configurations. In total we generated 6 (interfaces) \times 5 (thicknesses) \times 2 (with and without the top electrode) = 60 configurations. The 2.5 u.c.-thick slabs with the gold electrode are displayed in Figure 4.

The immediate observations from Figure 4 are that (i) all the interfaces have dimerized silicon, preserving the 2×1 periodicity of the Si(001) surface, and (ii) in 2 interfaces, there is migration of oxygen from the first SrO layer to the ZrO₂ layer (a full migration in *S1* and sharing of an oxygen between the two layers in *S5*). For all configurations, from the first (bottom) TiO₂ layer up to the top layer, STO possesses the stoichiometric perovskite structure. Therefore, while examining the polarization profile of these stacks, we start from the first TiO₂ layer.

2. Interfacial chemistry

In an oxide/semiconductor interface such as ZrO₂/Si, the chemical bonding at the interface is expected to determine the electronic structure of the stack, which then influences the polarization profile [9, 29]. A simple inspection of Figure 4 suggests that there are two types of ZrO₂/Si interfaces present: (1) where one of the atoms in the silicon dimer bonds with an oxygen (*S1* through *S5*), and (2) where both of the atoms in the silicon dimer bond with oxygens (*S6*). In both types, these bonds are between the dangling hybrid orbitals of Si (with sp^3 character) and the $2p_z$ orbitals of interfacial O. In Figure 5, we describe the interfacial chemistry for both types and use *S3* to represent the first type. The Si dangling hybrid orbitals are labeled h_1 and h_2 , and the participating oxygen p_z orbitals are labeled p_1 and p_2 . In the left panel, the interface geometries for (a) *S3* and (b) *S6* are displayed, with the schematics of participating orbitals overlaid on their respective atoms (for *S3*, p_1 does not significantly with h_1 , and hence does not participate).

For *S3*, prior to the formation of the interface, the oxygen atoms are in the O²⁻ state, thus p_2 starts out with two electrons, whereas h_1 and h_2 have one electron each (middle panel in Figure 5(a)). Once the interface is formed, two of the three electrons in the h_2 and p_2 orbitals occupy the (h_2p_2) bonding states, and the remaining electron is accepted by h_1 . In the right panel of Figure 5(a), we display the projected densities of states (PDOS) of these orbitals, before and after the interface is formed. We use Si $3p_z$ orbitals to approximate h_1 and h_2 since we expect these orbitals to be in close alignment with the z -axis for a dimerized surface. In the figure, we see that h_1 and h_2 are half-occupied before the interface is formed, and p_2 is fully occupied. After the interface is formed, h_2 mixes strongly with p_2 and their spectral fea-

tures become broad at low energies while the PDOS for h_1 becomes fully occupied without a significant change in its shape.

For *S6*, in contrast to *S3*, both p_1 and p_2 participate in the chemical bonding in the same way. After the formation of the (h_1p_1) and (h_2p_2) bonds, an electron per bond dopes the Fermi level, due to the absence of available unoccupied or partially occupied interface states. In the right panel of Figure 5(b), PDOS for h_1 and p_1 are displayed before and after the interface is formed (h_2 and p_2 are almost identical to their counterparts, and hence not shown). Upon the formation of the interface, h_1 and p_1 mix, the electrons are donated to the Fermi level, and the Fermi level enters the conduction band (see DOS of Figure 10(b)) indicating electron doping into the conduction band.

To further support our simple picture of the interfacial chemistry, we have computed the electron redistribution for (1.5 u.c. SrTiO₃)/ZrO₂/Si stacks, defined as $\Delta n(x, y, z) = n_{\text{STO/ZrO}_2/\text{Si}}(x, y, z) - n_{\text{STO/ZrO}_2}(x, y, z) - n_{\text{Si}}(x, y, z)$. We then average over the $1 \times$ direction and obtain $\overline{\Delta n}(x, z)$, which we display in Figure 6(a) and Figure 6(c) for *S3* and *S6*, respectively. For *S3*, the figure indicates that the electron density around the Si-O (h_2p_2) bond decreases while the density in the region between the un-bonded Si atom and the neighboring Zr atom increases. For *S6*, on the other hand, the electron density around the Si-O bonds decreases while the regions of increasing electron density are spatially distributed in the oxide. Plots analogous to Figure 6 for the remaining configurations (*S1*, *S2*, *S4* and *S5*) are presented in the Supplementary Material. The simple interfacial chemistry model we have obtained for *S3* also apply to these configurations.

We present the total energies of the considered films in Figure 7. The total energy of the *S1* configuration is taken as the reference for each case. We make two observations: (i) relative energies change with film thickness but generally stay within ± 0.1 eV once the STO thickness is above 2 u.c.; and (ii) the energy ordering is significantly affected by the inclusion of the gold electrode. The largest changes in relative energy with the addition of the electrode are for *S6* (approx. -0.7 eV) and *S3* (approx. -0.4 eV). These most stabilized interfaces are also the ones with the largest polarization enhancement when the electrode is added (Figure 8 and Figure 9). Therefore, a subset of the possible interfaces become especially stabilized by a high-work-function electrode such as gold. As we will discuss below, this stabilization occurs by an electron transfer to the electrode which was previously observed in the BaTiO₃/Ge system [9]. With the usage of the electrode with a finely tuned work function, the lowest energy interfaces (*S6* and *S3* in this case) can in principle be made degenerate, enabling polarization switching without an energy cost.

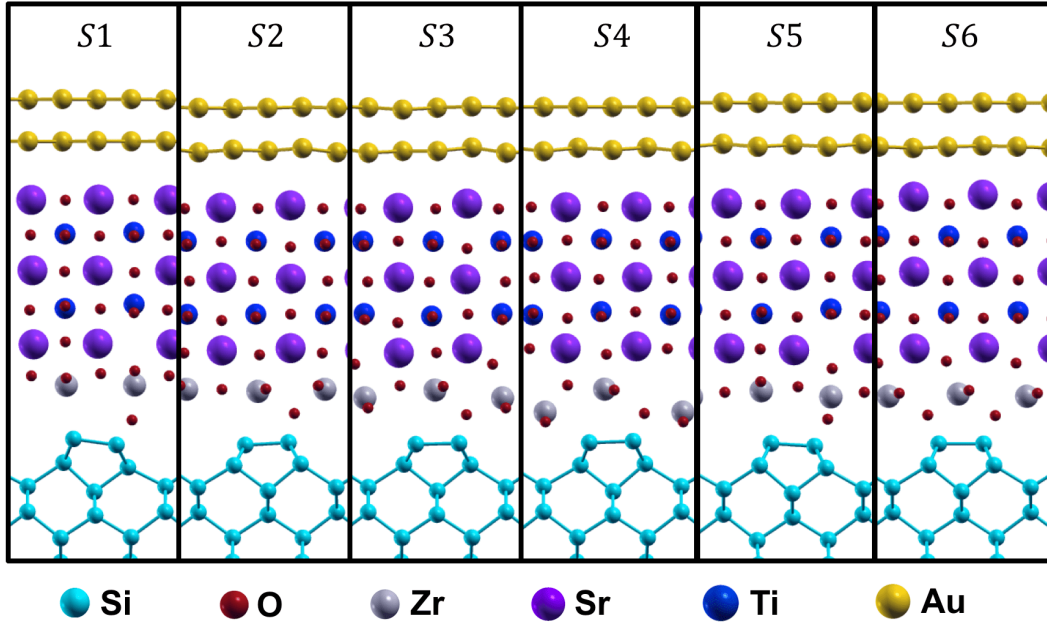


Figure 4. Relaxed $\text{SrTiO}_3/\text{ZrO}_2/\text{Si}$ heterostructures with 2.5 u.c.-thick STO and Au top electrode. For each configuration, the displayed portion of the stack is slightly larger than the 2×1 unit cell.

3. Film polarization

In order to assess the possibility of ferroelectric switching in the $\text{SrTiO}_3/\text{ZrO}_2/\text{Si}$ stacks, we have computed the layer-by-layer mean vertical cation-anion separation: $\delta z \equiv z(\text{Sr or Ti}) - z(\text{O})$ where the averaging is done over a layer. We present the polarization profile of 3.5 u.c.-thick SrTiO_3 films in Figure 8, starting with the bottom TiO_2 layer. We observe that for the films without a top electrode (Figure 8(a)), the polarization at the surface SrO layer is pinned to the same value for all interface configurations, shrinking the variation of the polarization among the configurations in the upper layers. We also see that generally the δz values near the ZrO_2 are larger and quickly decay toward the middle STO layers. This is due to the depolarizing field not being screened by mobile charges or a capping electrode. When the electrode is added, the depolarizing field is screened by the metal, the top SrO polarization is no longer pinned, and thus varies with the interface configuration (Figure 8(b)). Furthermore, the polarization values for each interface increases with the capping electrode. This can be explained by a high-work-function electrode such as Au pulling mobile electrons from the $\text{STO}/\text{ZrO}_2/\text{Si}$ system, thereby creating an electric field that attracts cations and repels anions. This effect is the largest in $S6$, which also has the largest polarization values for non-capped systems in Figure 8(a), indicating that these interfaces have more mobile carriers in them. This is in agreement with our discussion above regarding the interfacial chemistry

of these configurations. These mobile carriers both (a) screen the depolarizing field in the absence of an electrode, causing the film to have larger polarization values, and (b) migrate to the capping electrode, further enhancing the ionic polarization.

We report the average polarization for all the films we have computed in Figure 9. A universal feature of these results is that the oxide's surface termination causes a small modulation in the average polarization, due to the pinning of the surface polarization to different values. For the films with no electrode (Figure 9(a)), the average polarization is close to zero, and does not significantly change with thickness, with the exception of $S6$. Regarding $S6$, because it has positive polarization values in the interior of STO but a negative value at the pinned surface layer, its average polarization value increases with increased thickness. As for the films with the capping electrode (Figure 9(b)), the charge transfer to the electrode causes all structures to have positive average polarizations that do not significantly depend on the thickness, again with the exception of $S6$. For this configuration, there is a slight downward slope for the average polarization when the thickness is increased. Our findings on polarization profiles and electrode effects are in line with previous studies on SrTiO_3/Si [29] and BaTiO_3/Ge interfaces [9].

A comparison of the polarization values with and without the gold electrode in Figure 8 and Figure 9 indicates the critical role of the top electrode in the enhancement of the variation in the ionic polarization among the stable configurations. To investigate the effect of

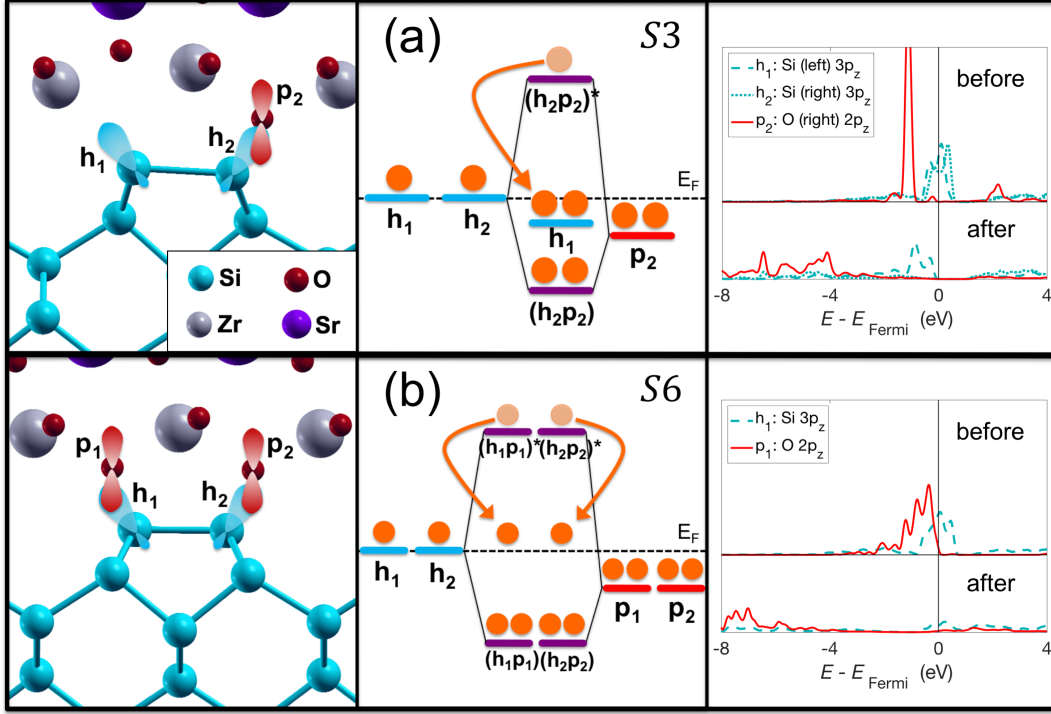


Figure 5. Chemical bonding at the ZrO_2/Si interface for $\text{SrTiO}_3/\text{ZrO}_2/\text{Si}$ stacks in the configurations (a) $S3$ and (b) $S6$. For each configuration, the atomic structure in the vicinity of this interface, as well as the schematics that represent the atomic orbitals participating in the chemical bonding are displayed in the left panel (see text for details); a level diagram that summarizes the simplified chemical bonding model of the interface is displayed in the middle panel; and densities of states projected onto the relevant atomic orbitals (PDOS) before and after the interface is formed are displayed in the right panel (only h_1 and p_1 are shown for $S6$ because of their approximate equivalence to h_2 and p_2 in this configuration). For the PDOS plots, the zero of the energy is taken as the Fermi level.

the electrode, we have computed the electron redistribution for $\text{SrTiO}_3/\text{ZrO}_2/\text{Si}$ stacks with 1.5 u.c.-thick STO, defined as $\Delta n(x, y, z) = n_{\text{Au}/\text{STO}/\text{ZrO}_2/\text{Si}}(x, y, z) - n_{\text{STO}/\text{ZrO}_2/\text{Si}}(x, y, z) - n_{\text{Au}}(x, y, z)$. Averaging over the $1 \times$ direction, we obtain $\overline{\Delta n}(x, z)$, which is shown in Figure 6(b) and Figure 6(d) for $S3$ and $S6$, respectively. In the figure, it is observed that in both configurations, a charge transfer from the oxide to the electrode occurs. This charge transfer is observed to be slightly more pronounced in $S6$. To quantify the charge transfer, we further average $\overline{\Delta n}(x, z)$ over the $2 \times$ direction to obtain $\overline{\Delta n}(z)$. Computing the integral of $\overline{\Delta n}(z)$ up to the electrode/oxide interface yields the total electron transfer per 2×1 unit cell, which are 0.21, 0.23, 0.22, 0.22, 0.23 for $S1$ through $S5$, respectively, and 0.26 for $S6$. Plots analogous to Figure 6 for the remaining configurations are presented in the Supplementary Material.

To further illustrate the chemical difference between the two types of interfaces ($S1$ through $S5$ versus $S6$) and the effect of the electrode, we have computed densities of states for (1.5 u.c. SrTiO_3)/ ZrO_2/Si with and

without the capping Au electrode. Our results are presented in Figure 10. In order to exclude the electrode states and focus on the oxide/semiconductor stack itself, we have summed the PDOS for all the Si, O, Zr, Sr and Ti atoms. We see that prior to the addition of the electrode, $S3$ and $S6$ have similar DOS curves except for the position of the Fermi level: $S3$ is a small-gap semiconductor whereas the Fermi level of $S6$ is in the conduction band. When the electrode is added, $S3$ becomes lightly hole doped (h_1 loses electrons and becomes partially filled when the electrode is added). For $S6$, the addition of the electrode suppresses the DOS at and around the Fermi level. Therefore the electron transfer mechanism in these two configurations are different: hole doping of interfacial states in $S3$ and reduction in the electron doping of the conduction band in $S6$. The plots corresponding to the remaining configurations are presented in the Supplementary Material. Because $S3$ and $S6$ are the two lowest-energy configurations (Figure 7) and have a large difference in ionic polarization (Figure 9), ferroelectric switching between them is in principle possible. Accord-

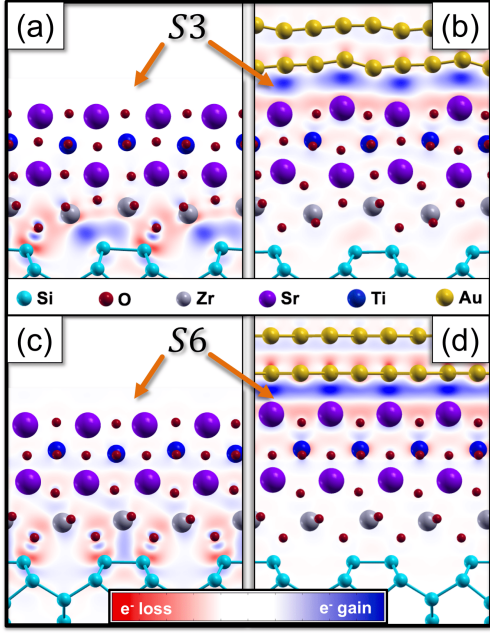


Figure 6. Electron density redistribution for (1.5 u.c. SrTiO_3)/ ZrO_2 /Si heterostructures upon the formation of the ZrO_2 /Si interface for the (a) $S3$ and (c) $S6$ configurations; and upon the addition of the capping electrode for the (b) $S3$ and (d) $S6$ configurations. The plots are obtained by averaging the electron density redistribution along the $1 \times$ direction.

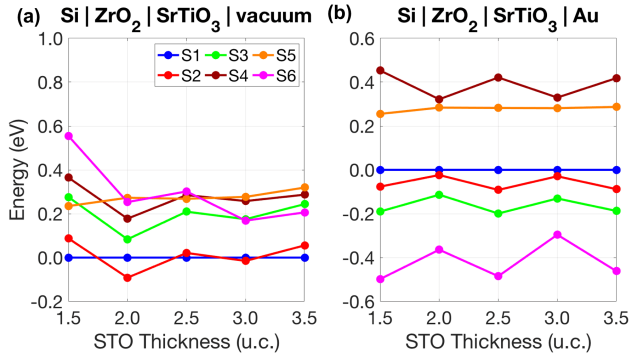


Figure 7. Energies of the SrTiO_3 / ZrO_2 /Si heterostructures with respect to the $S1$ configuration vs STO thickness, (a) without a top electrode, and (b) with Au as the top electrode. The energy is given in eV per 2×1 unit cell.

ing to our analysis, this switching would be accompanied by a modulation of the interfacial chemistry, between hole doping and electron doping, analogous to the BaTiO_3 /Ge interface [9].

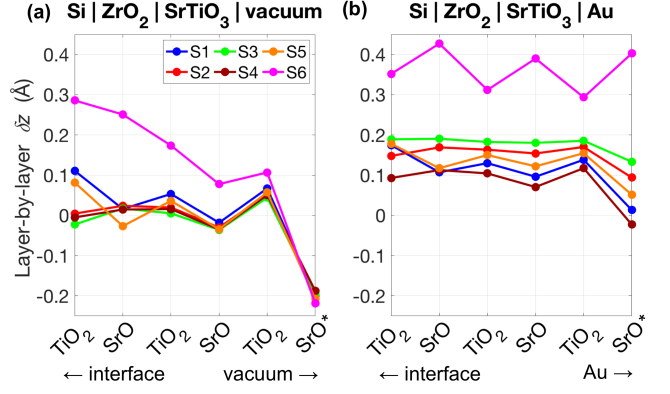


Figure 8. Layer-by-layer polarization profile, measured by mean vertical cation-anion separation (δz) within a layer for 3.5 u.c.-thick STO films in SrTiO_3 / ZrO_2 /Si heterostructures, (a) without a top electrode, and (b) with Au as the top electrode. The top SrO layer (farthest from the interface) is marked with an asterisk for both cases.

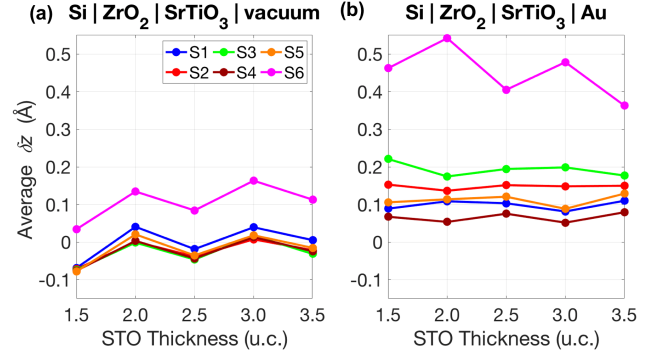


Figure 9. Average polarization, measured by taking the average of δz for all the layers in a given film, vs STO thickness in SrTiO_3 / ZrO_2 /Si heterostructures, (a) without a top electrode, and (b) with Au as the top electrode.

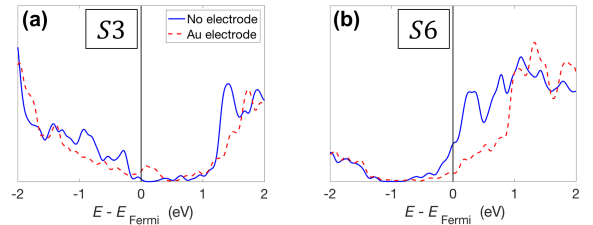


Figure 10. Densities of states (DOS) for (1.5 u.c. SrTiO_3)/ ZrO_2 /Si heterostructures with and without the top Au electrode for (a) $S3$ and (b) $S6$ configurations. These DOS is approximated by summing the projected DOS (PDOS) for all Si, O, Zr, Sr and Ti Löwdin orbitals in the stack (excluding Au if present). The zero of the energy is taken as the Fermi level for each case.

IV. CONCLUSION

We have conducted a density functional theory investigation of the oxygen content for ZrO_x monolayers on silicon where $x = 1.0, 1.5, 2.0, 2.5, 3.0$. We have found that the multiplicity of low-energy structures obtained in ZrO_2 is preserved for both under- and over-oxygenated monolayers. Our results indicate that $\text{ZrO}_{1.5}$ and $\text{ZrO}_{2.5}$ may also be used as a ferroelectric oxide with potentially larger polarization switching. We have also presented our examination of ZrO_2 as a buffer layer between Si and SrTiO_3 . We have found that $\text{SrTiO}_3/\text{ZrO}_2/\text{Si}$ systems possess multiple atomic configurations with different polarization profiles within a 1 eV energy window. We have also shown that the relative energies of these structures can be significantly changed with the help of a top electrode. Using an electrode with the right work function, two low-energy structures can be brought energetically close, which may allow for polarization switching that does not involve high-energy metastable structures. This suggests that ZrO_2 may be used as an atomically-thin buffer layer to induce switchable polarization in a thicker perovskite film on silicon. If this system is experimentally realized and shown to have the desired transport properties, it will present an attractive alternative in the field of non-volatile devices. The main trends in our report may also guide future theoretical and experimental research into monolayer oxides and their heterostructures.

V. ACKNOWLEDGEMENTS

This work was supported primarily by the grant NSF MRSEC DMR-1119826. We thank the Yale Center for Research Computing for guidance and use of the research computing infrastructure, with special thanks to Stephen Weston and Andrew Sherman. Additional computational support was provided by NSF XSEDE resources via Grant TG-MCA08X007.

-
- [1] M. Dogan, S. Fernandez-Peña, L. Kornblum, Y. Jia, D. P. Kumah, J. W. Reiner, Z. Krivokapic, A. M. Kolpak, S. Ismail-Beigi, C. H. Ahn, et al., *Nano Letters* **18**, 241 (2018), ISSN 1530-6984, URL <http://dx.doi.org/10.1021/acs.nanolett.7b03988>.
 - [2] M. Dogan and S. Ismail-Beigi, arXiv:1902.01022 [cond-mat] (2019), arXiv: 1902.01022, URL <http://arxiv.org/abs/1902.01022>.
 - [3] H. Y. Hwang, Y. Iwasa, M. Kawasaki, B. Keimer, N. Nagaosa, and Y. Tokura, *Nature Materials* **11**, 103 (2012), ISSN 1476-1122, URL <http://www.nature.com/nmat/journal/v11/n2/abs/nmat3223.html>.
 - [4] J. Mannhart and D. G. Schlom, *Science* **327**, 1607 (2010), ISSN 0036-8075, 1095-9203, URL <http://science.sciencemag.org/content/327/5973/1607>.
 - [5] R. A. McKee, F. J. Walker, and M. F. Chisholm, *Science* **293**, 468 (2001), ISSN 0036-8075, 1095-9203, URL <http://www.sciencemag.org/content/293/5529/468>.
 - [6] K. F. Garrity, A. M. Kolpak, and S. Ismail-Beigi, *Journal of Materials Science* **47**, 7417 (2012), ISSN 0022-2461, 1573-4803, URL <http://link.springer.com/article/10.1007/s10853-012-6425-z>.
 - [7] J. W. Reiner, F. J. Walker, and C. H. Ahn, *Science* **323**, 1018 (2009), ISSN 0036-8075, 1095-9203, URL <http://www.sciencemag.org/content/323/5917/1018>.
 - [8] J. W. Reiner, A. M. Kolpak, Y. Segal, K. F. Garrity, S. Ismail-Beigi, C. H. Ahn, and F. J. Walker, *Advanced Materials* **22**, 2919 (2010), ISSN 1521-4095, URL <http://onlinelibrary.wiley.com/doi/10.1002/adma.200904306/abstract>.
 - [9] M. Dogan and S. Ismail-Beigi, *Physical Review B* **96**, 075301 (2017), URL <https://link.aps.org/doi/10.1103/PhysRevB.96.075301>.
 - [10] I. P. Batra, P. Wurfel, and B. D. Silverman, *Physical Review B* **8**, 3257 (1973), URL <http://link.aps.org/doi/10.1103/PhysRevB.8.3257>.
 - [11] C. Dubourdieu, J. Bruley, T. M. Arruda, A. Posadas, J. Jordan-Sweet, M. M. Frank, E. Cartier, D. J. Frank, S. V. Kalinin, A. A. Demkov, et al., *Nature Nanotechnology* **8**, 748 (2013), ISSN 1748-3387, URL <http://www.nature.com/nnano/journal/v8/n10/full/nnano.2013.192.html>.
 - [12] J. Robertson, *Reports on Progress in Physics* **69**, 327 (2006), ISSN 0034-4885, URL <http://iopscience.iop.org/0034-4885/69/2/R02>.
 - [13] M. D. McDaniel, T. Q. Ngo, A. Posadas, C. Hu, S. Lu, D. J. Smith, E. T. Yu, A. A. Demkov, and J. G. Ekerdt, *Advanced Materials Interfaces* **1**, n/a (2014), ISSN 2196-7350, URL <http://onlinelibrary.wiley.com/doi/10.1002/admi.201400081/abstract>.
 - [14] R. A. McKee, F. J. Walker, and M. F. Chisholm, *Physical Review Letters* **81**, 3014 (1998), URL <http://link.aps.org/doi/10.1103/PhysRevLett.81.3014>.
 - [15] D. P. Kumah, M. Dogan, J. H. Ngai, D. Qiu, Z. Zhang, D. Su, E. D. Specht, S. Ismail-Beigi, C. H. Ahn, and F. J. Walker, *Physical Review Letters* **116**, 106101 (2016), URL <http://link.aps.org/doi/10.1103/PhysRevLett.116.106101>.
 - [16] A. M. Kolpak and S. Ismail-Beigi, *Physical Review B* **83**, 165318 (2011), URL <http://link.aps.org/doi/10.1103/PhysRevB.83.165318>.
 - [17] W. Xiao, C. Liu, Y. Peng, S. Zheng, Q. Feng, C. Zhang, J. Zhang, Y. Hao, M. Liao, and Y. Z. g, *IEEE Electron Device Letters* pp. 1–1 (2019), ISSN 0741-3106, URL <https://ieeexplore.ieee.org/document/8662670>.
 - [18] J. P. Perdew, K. Burke, and M. Ernzerhof, *Physical Review Letters* **77**, 3865 (1996), URL <http://link.aps.org/doi/10.1103/PhysRevLett.77.3865>.
 - [19] D. Vanderbilt, *Physical Review B* **41**, 7892 (1990), URL <http://link.aps.org/doi/10.1103/PhysRevB.41.7892>.
 - [20] P. Giannozzi, S. Baroni, N. Bonini, M. Calandra, R. Car, C. Cavazzoni, Davide Ceresoli, G. L. Chiarotti, M. Cococcioni, I. Dabo, et al., *Journal of Physics: Condensed Matter* **21**, 395502 (2009), ISSN 0953-8984, URL <http://stacks.iop.org/0953-8984/21/i=39/a=395502>.
 - [21] N. Marzari, D. Vanderbilt, A. De Vita, and M. C. Payne, *Physical Review Letters* **82**, 3296 (1999), URL <http://link.aps.org/doi/10.1103/PhysRevLett.82.3296>.

- [22] L. Bengtsson, Physical Review B **59**, 12301 (1999), URL <http://link.aps.org/doi/10.1103/PhysRevB.59.12301>.
- [23] Y. Miyamoto and A. Oshiyama, Physical Review B **41**, 12680 (1990), URL <http://link.aps.org/doi/10.1103/PhysRevB.41.12680>.
- [24] T. Uchiyama and M. Tsukada, Surface Science **357–358**, 509 (1996), ISSN 0039-6028, URL <http://www.sciencedirect.com/science/article/pii/0039602896800768>.
- [25] C. Kittel, *Introduction to Solid State Physics* (Wiley, 2004), ISBN 978-0-471-41526-8, URL <https://books.google.com/books?id=kym4QgAACAAJ>.
- [26] J. Heyd, J. E. Peralta, G. E. Scuseria, and R. L. Martin, The Journal of Chemical Physics **123**, 174101 (2005), ISSN 0021-9606, URL <https://aip.scitation.org/doi/10.1063/1.2085170>.
- [27] A. M. Kolpak, F. J. Walker, J. W. Reiner, Y. Segal, D. Su, M. S. Sawicki, C. C. Broadbridge, Z. Zhang, Y. Zhu, C. H. Ahn, et al., Physical Review Letters **105**, 217601 (2010), URL <http://link.aps.org/doi/10.1103/PhysRevLett.105.217601>.
- [28] J. H. Haeni, P. Irvin, W. Chang, R. Uecker, P. Reiche, Y. L. Li, S. Choudhury, W. Tian, M. E. Hawley, B. Craigo, et al., Nature **430**, 758 (2004), ISSN 0028-0836, URL <http://www.nature.com/nature/journal/v430/n7001/full/nature02773.html>.
- [29] A. M. Kolpak and S. Ismail-Beigi, Physical Review B **85**, 195318 (2012), URL <http://link.aps.org/doi/10.1103/PhysRevB.85.195318>.

Supplementary Material for “Ferroelectric ZrO₂ monolayers as buffer layers between SrTiO₃ and Si”

Mehmet Dogan^{1,2,3,4} and Sohrab Ismail-Beigi^{1,2,5,6}

¹Center for Research on Interface Structures and Phenomena, Yale University, New Haven, Connecticut
06520, USA

²Department of Physics, Yale University, New Haven, Connecticut 06520, USA

³Department of Physics, University of California, Berkeley, California 94720, USA

⁴Materials Science Division, Lawrence Berkeley National Laboratory, Berkeley, California 94720, USA

⁵Department of Applied Physics, Yale University, New Haven, Connecticut 06520, USA

⁶Department of Mechanical Engineering and Materials Science, Yale University, New Haven, Connecticut
06520, USA

Low-energy ZrO_x configurations

O:Zr = 1.0

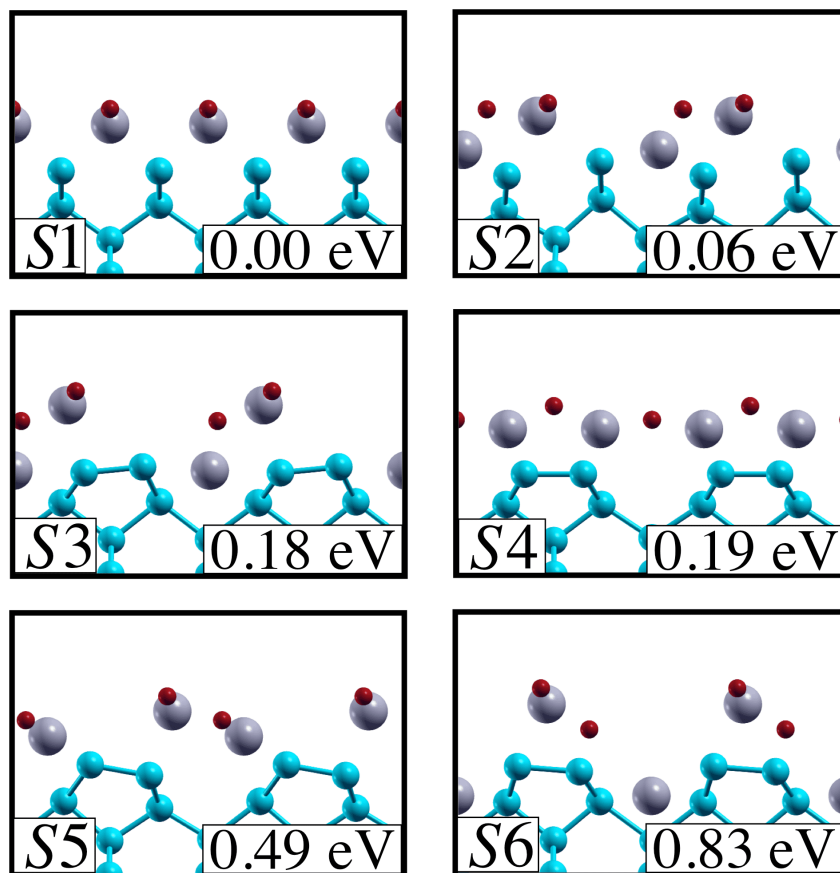


Figure 1: Low-energy relaxed configurations of monolayers with $\text{O:Zr} = 1.0$. Energies are per 2×1 in-plane cell.

O:Zr = 1.5

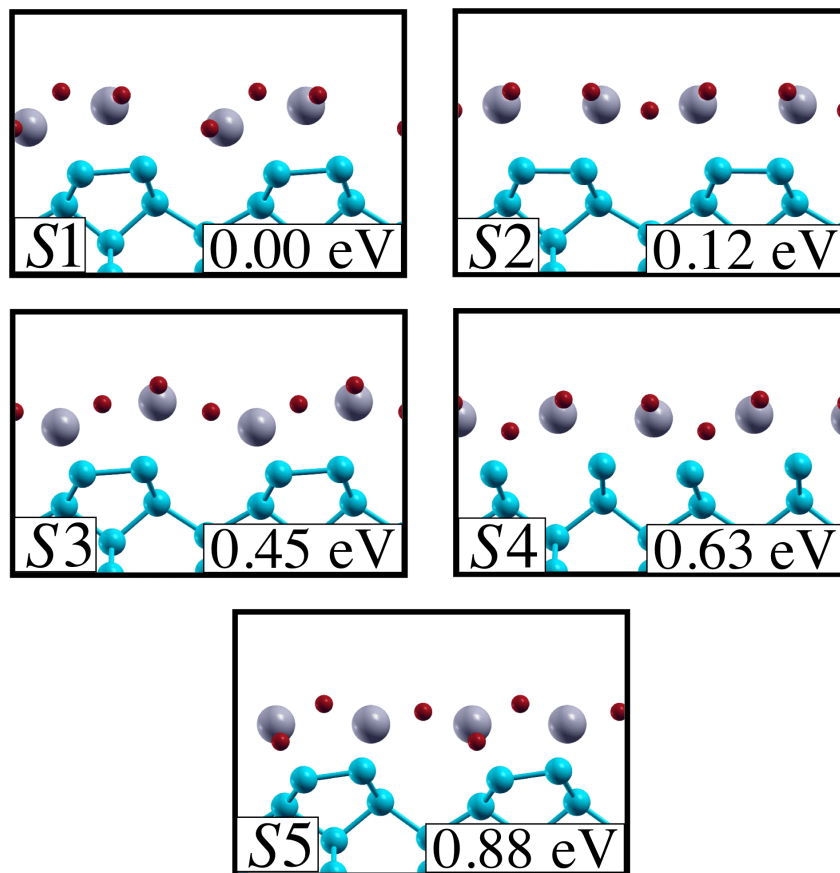


Figure 2: Low-energy relaxed configurations of monolayers with O:Zr = 1.5. Energies are per 2×1 in-plane cell.

O:Zr = 2.5

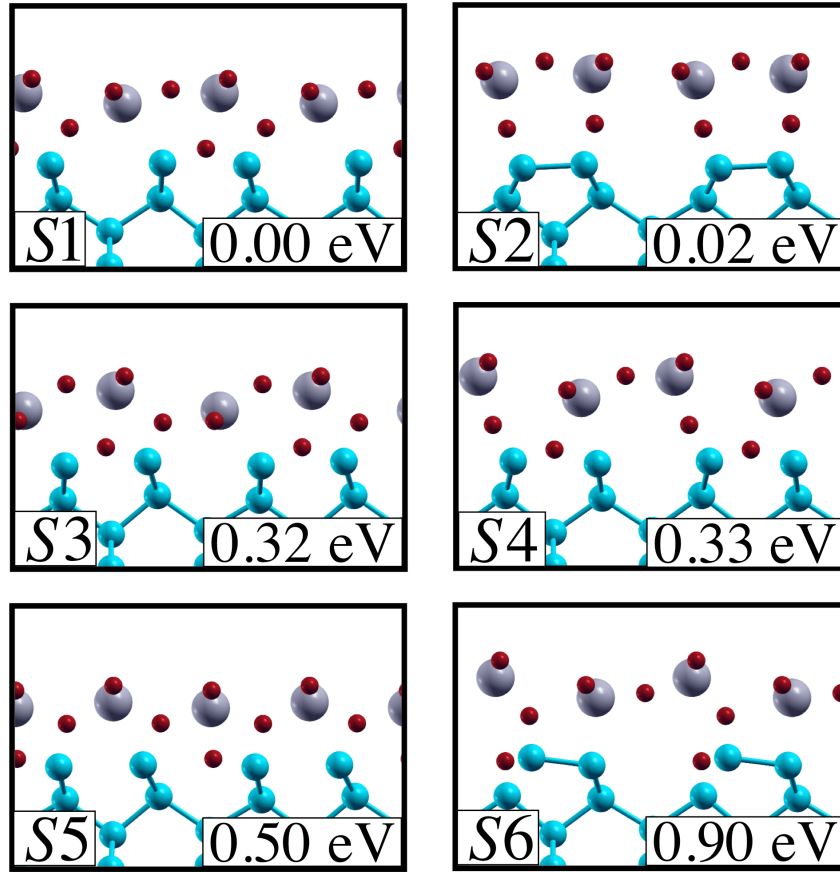


Figure 3: Low-energy relaxed configurations of monolayers with O:Zr = 2.5. Energies are per 2×1 in-plane cell.

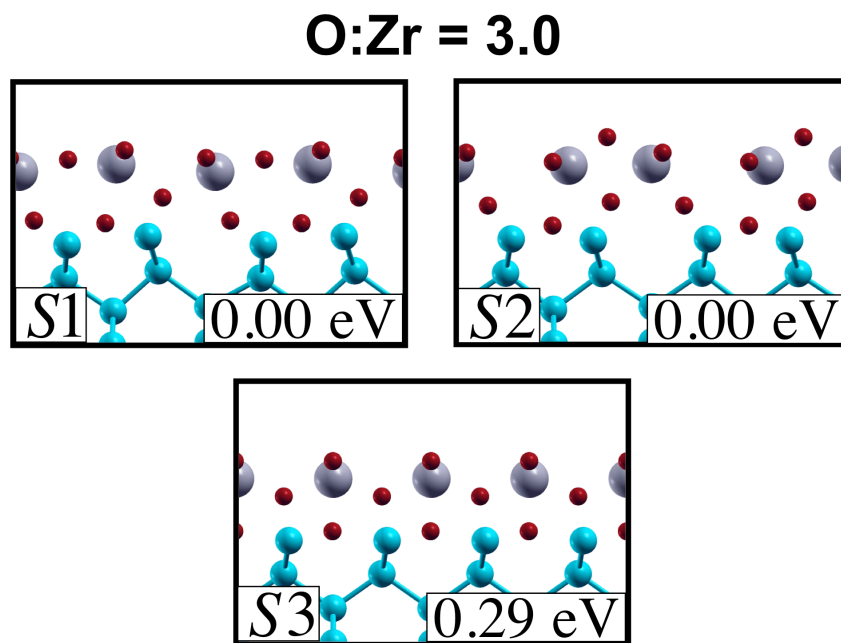


Figure 4: Low-energy relaxed configurations of monolayers with $\text{O:Zr} = 3.0$. Energies are per 2×1 in-plane cell.

Electronic structure of $\text{SrTiO}_3/\text{ZrO}_2/\text{Si}$ stacks

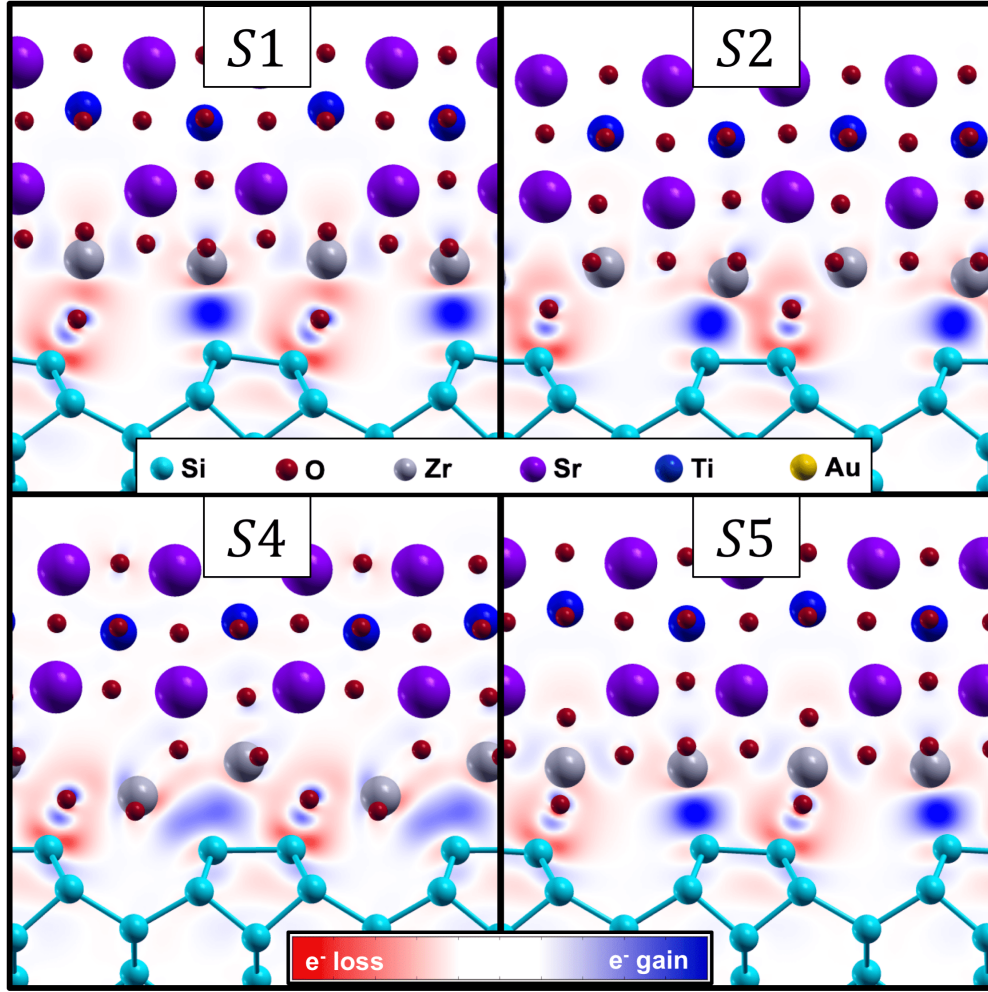


Figure 5: Electron density redistribution for $(1.5 \text{ u.c. SrTiO}_3)/\text{ZrO}_2/\text{Si}$ heterostructures upon the formation of the ZrO_2/Si interface for $S1$, $S2$, $S4$ and $S5$ configurations.

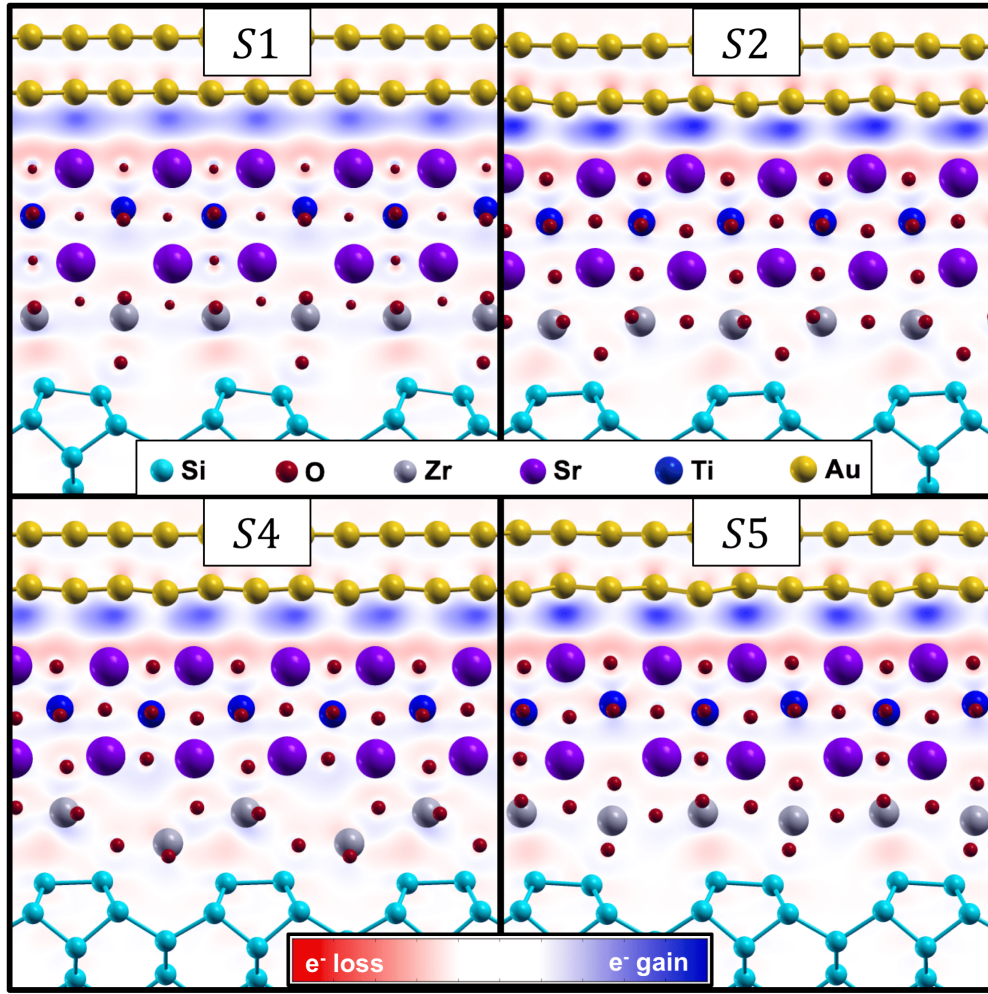


Figure 6: Electron density redistribution for (1.5 u.c. SrTiO₃)/ZrO₂/Si heterostructures upon the addition of the top Au electrode for *S1*, *S2*, *S4* and *S5* configurations.

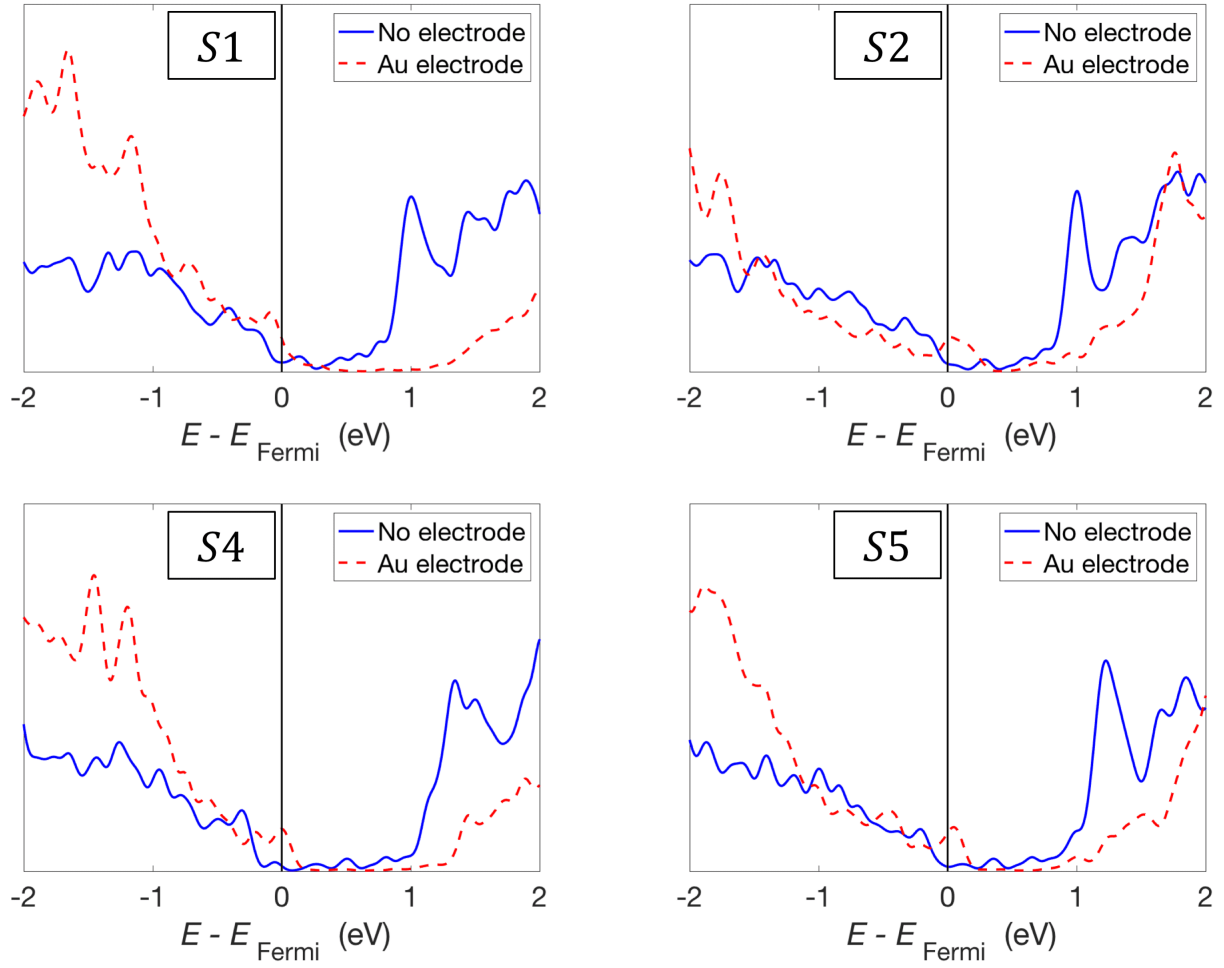


Figure 7: Densities of states (DOS) for (1.5 u.c. SrTiO_3)/ ZrO_2 /Si heterostructures with and without the top Au electrode for $S1$, $S2$, $S4$ and $S5$ configurations. The total DOS is approximated by summing the PDOS for all the Si, O, Zr, Sr and Ti atoms in the stack (thereby excluding the Au states). The zero of the energy is taken as the Fermi level for each case.